AIAA JOURNAL
Vol. 48, No. 8, August 2010

Effects of Injection and Main Flow Conditions on Supersonic Turbulent Mixing Structure

Hidemi Takahashi* and Goro Masuya†
Tohoku University, Sendai 980-8579, Japan
and
Mitsutomo Hirota‡
Muroran Institute of Technology, Muroran 050-8585, Japan

DOI: 10.2514/1.J050355

The effects of injection and main flow conditions on the turbulent structure produced by a gaseous sonic transverse injection into a supersonic airstream were investigated. The turbulent structure inherent in the mixing flowfield was characterized by the single-time two-point spatial correlations based on the concentration fluctuation and measured with acetone planar laser-induced fluorescence. Results revealed that the most intensively fluctuating region appeared on the 50%-averaged-concentration track, irrespective of the injection conditions. The highly correlated region, which indicates an organized large-scale structure, appeared as a tilting ellipse in the lower-compressibility cases and an ellipse almost parallel to the streamline in the higher-compressibility cases. These differences in structure result in the difference of the averaged jet width. The injection with the higher-compressibility condition showed more stable structures and slower development in the size due to suppression of the instability growth. The structure was likely to be stretched toward the averaged-velocity direction as the main flow Mach number increased. Increasing the velocity difference between the jet and main flow caused the large-scale eddies to appear more frequently.

Nomenclature

a	=	speed of sound, m/s
C	=	molar concentration, mol/m^3
D	=	diameter of injection port, m
D_{eq}	=	equivalent diameter of the fitted ellipse, m
J	=	jet-to-mainstream momentum flux ratio
M	=	Mach number
M_c	=	convective Mach number
m	=	molecular weight, kg/mol
P	=	local static pressure, Pa
r	=	spatial correlation factor
T	=	local static temperature, K
x	=	streamwise coordinate, m
y	=	transverse coordinate, m
z	=	spanwise coordinate, m
γ	=	specific heat ratio
ρ	=	density, kg/m^3
χ	=	mole fraction

Subscripts

j	=	jet
m	=	main flow

I. Introduction

DETAILED understanding of the turbulent mixing mechanisms in the supersonic flowfield is necessary for designing a successful scramjet injector. Recent studies with a highly resolved visualization technique, such as acetone planar laser-induced fluorescence (PLIF), indicated the existence of large-scale vortex structures, even in a high-speed flow with injection [1,2]. The flowfield was investigated from several points of view with instantaneous, mean, standard deviation (STD), and intensity probability density functions. As a result, qualitative features of the flowfield generated by turbulent structures were revealed. The main role of the turbulent structure may be large-scale stirring between jet fluids and crossflow fluids before the molecular-scale mixing relating to the combustion. However, owing to the complex features of the flowfield, such as high compressibility and three-dimensionality resulting in difficulties in direct precise measurement, quantitative turbulent behavior has not been well clarified, and the compressibility effects to the turbulent structure have not been revealed as well. Further investigation is necessary. To characterize the turbulent behavior, the single-time two-point spatial correlations based on the concentration fluctuation were calculated by the present authors [1]. Their result revealed several important geometrical characteristics, such as shape, size, orientation, and appearance intervals of the large-scale vortex structures for a single set of main flow and injection conditions.

In this study, we focus on the behavior of the large-scale structure and the compressibility effects for various conditions of the main flow and injection. By changing the flow conditions, effects of the jet-to-mainstream momentum flux ratio J, the main flow Mach number M_m, and the injectant molecular weight m_j on the development of the turbulent structure are examined. Since J [related to Mach numbers, stagnation pressures, and specific heat ratios of the main and injectant flows, as expressed by Eq. (1)] is a very classical parameter for injection, its effects on penetration height, concentration profiles, and other time-averaged dynamic features of the jet have been investigated fairly well [3,4]:

$$J = \frac{(\gamma p M^2)_j}{(\gamma p M^2)_m} = \left(\frac{\gamma_j}{\gamma_m}\right) \cdot \left(\frac{M_j}{M_m}\right)^2 \cdot \left(\frac{p_{0j}}{p_{0m}}\right) \cdot \left\{\frac{(1 + [(\gamma_j - 1)/2]M_j^2)^{-\gamma_j/(\gamma_j - 1)}}{(1 + [(\gamma_m - 1)/2]M_m^2)^{-\gamma_m/(\gamma_m - 1)}}\right\} \tag{1}$$

However, the influence of J on the turbulent structure is still poorly understood. In addition, effects of the main flow Mach number and

Presented as Paper 2009-7408 at the 16th AIAA/DLR/DGLR International Space Planes and Hypersonic Systems and Technologies Conference, Bremen, Germany, 19–22 October 2009; received 22 November 2009; revision received 1 March 2010; accepted for publication 12 March 2010.

*Japan Society for the Promotion of Science Research Fellow, Department of Aerospace Engineering; currently Postdoctoral Fellow at Department of Mechanical and Aerospace Engineering, University of Florida. Member AIAA.
†Professor, Department of Aerospace Engineering. Senior Member AIAA.
‡Lecturer, Department of Mechanical Systems Engineering.

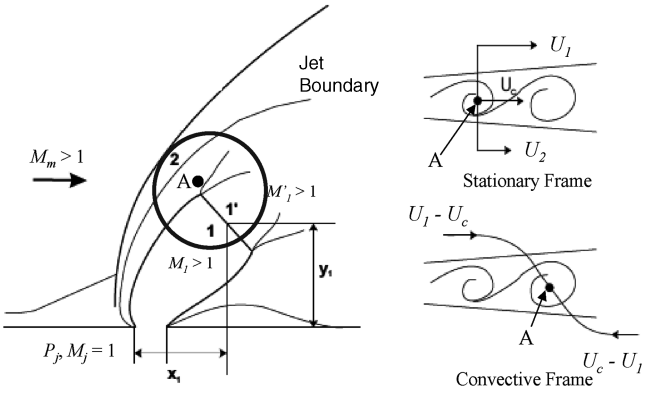

Fig. 1 Flowfield schematics used in the jet compressibility analysis. Letter A indicates the zone of the jet shear layer [5].

the injectant molecular weight are not fully understood either. In the operational condition of the scramjet, J and M_m vary with the flight Mach number. In accordance with those changes, the flow state and turbulent structure in the combustor will change. Hence, these effects on the turbulent structure must be investigated to achieve high mixing and combustion performance of the scramjet combustor. To estimate the compressibility effects on the turbulent mixing of the simple two-stream mixing layer, the convective Mach numbers are used:

$$M_{c1} = \frac{U_1 - U_c}{a_1}; \qquad M_{c2} = \frac{U_c - U_2}{a_2} \tag{2}$$

where U_1 and U_2 are the velocity of high- and low-speed streams, respectively, and U_c is a convective speed of the large-scale structure. For the present experimental configuration of transverse injection from the wall orifice, Gruber et al. [5] proposed a model to evaluate these parameters. The main flow Mach number and the injectant sonic speed or its molecular weight appeared in their model, and they might be influential to the turbulent structure through the compressibility of the flow. So, we chose them for parametric investigation as well.

The investigations were conducted with the aid of acetone PLIF visualization for various experimental conditions. The single-time two-point spatial correlations of fluorescence intensity fluctuation were calculated to characterize the scalar turbulent structures.

II. Experimental Apparatus and Data Analysis

A. Wind Tunnel, Flowfield Conditions, and Acetone Planar Laser-Induced Fluorescence

The suction-type wind tunnel, which is the same one as used in our previous studies [1,6,7], provided an unheated supersonic airstream in the 200-mm-long test section, with a 30 mm^2 constant cross section. The nominal Mach numbers of the main flow were 2.0 and 2.5, with replaceable nozzles. Experiments with subsonic main flow, for which the Mach number was 0.91 (determined from wall pressure), were done as well for comparison. The injection conditions were parametrically changed. Gaseous air or helium (He) at room temperature was used as an injectant to vary the jet molecular weight and was transversely injected at a sonic condition from a circular orifice with a 2.5 mm diameter D on a wall of the test section. The jet-to-mainstream momentum flux ratio J was controlled by varying the injection pressure. Convective Mach numbers (M_{c1} and M_{c2}) for estimating an initial compression level of the flow were calculated at point A in Fig. 1, using Gruber et al.'s model [5]. The detailed flow conditions with their uncertainties are summarized in Table 1.

The flowfield was optically measured with acetone PLIF. The light source was fourth-harmonic radiation from a Q-switched pulsed neodymium-doped–yttrium-aluminum-garnet laser with a wavelength of 266 nm, energy of 70 mJ/pulse, and the maximum repetition rate of 10 Hz. The fluorescence images were recorded using a charge-coupled device camera with a 1024×1024 array of square pixels. The spatial resolution was 36.8 μm/pixel. Acetone vapor, a tracer for PLIF, was seeded only in the injectant. The density change of injectant due to acetone seeding was estimated to be less than 1.4%, and this level of acetone seeding caused a negligible influence on the injectant behavior. Further details of the experimental apparatus, flow conditions, and instrumentation are described in [4].

B. Uncertainty Analysis

For the LIF measurement, the overall uncertainty inherent in each fluorescence data point in each pixel, associated with the elements of error sources tabulated in Table 2, was estimated to be 3.3%. This number is translated directly into a relative uncertainty in the fluorescence signal at the same amount.

C. Single-Time Two-Point Spatial Correlation Analysis Using Acetone Planar Laser-Induced Fluorescence Data

The fluorescence signal from acetone molecules S is almost proportional to the acetone molar concentration C_{acetone} (mol/m^3) for the present experiment conditions, with a range of $\pm 6.0\%$ of error [7], and is expressed as follows:

$$S = \text{const} \cdot \frac{\chi_{\text{acetone}} \cdot \rho_{\text{mixture}}}{m_{\text{mixture}}} = \text{const} \cdot C_{\text{acetone}} = \text{const} \cdot \chi_{\text{acetone}_j} \cdot C_j \tag{3}$$

where the seeding mole fraction of acetone in the injectant χ_{acetone} is constant. Clearly, the PLIF signal intensity is proportional to the injectant concentration. Therefore, the spatial correlation based on the PLIF signal fluctuations provides the spatial features of the turbulent field represented by the scalar fluctuation.

The single-time two-point spatial correlation $r(x, y, \Delta x, \Delta y)$ based on the concentration fluctuation was computed by Eq. (4):

Table 1 Summary of the operating conditions used in this study

Case	Injectant	J	M_m	P_{0m}	T_{0m}	P_{0j}, kPa	T_{0j}	M_{c1}	M_{c2}
1	Air	1.86 ± 0.02	2.0	99.53 ± 0.01	296	189.23 ± 1.47	296	0.52	0.93
2		1.88 ± 0.01	2.5	99.59 ± 0.01	291	133.86 ± 0.42	291	0.33	0.55
3		2.80 ± 0.05	2.0	100.07 ± 0.22	291	285.63 ± 4.28	291	0.54	1.12
4		2.77 ± 0.04	2.5	99.47 ± 0.72	292	196.56 ± 3.11	292	0.31	0.75
5	He	1.91 ± 0.04	2.0	99.21 ± 0.49	294	176.14 ± 3.39	294	1.71	1.72
6		1.87 ± 0.01	2.5	99.61 ± 0.22	291	121.21 ± 0.71	291	1.64	1.67
7		2.78 ± 0.03	2.0	100.13 ± 0.58	293	256.56 ± 2.38	293	1.86	2.16
8		2.80 ± 0.05	2.5	99.98 ± 0.02	293	181.54 ± 3.01	293	1.78	2.14
9	Air	1.65 ± 0.02	0.91	99.69 ± 0.02	295	139.61 ± 0.69	295	——	——
10		2.25 ± 0.07		99.65 ± 0.01	295	204.50 ± 2.03	295	——	——
11	He	1.53 ± 0.01	0.91	99.77 ± 0.05	295	130.92 ± 1.30	295	——	——
12		2.24 ± 0.02		99.68 ± 0.01	297	187.02 ± 4.07	297	——	——

Table 2 Uncertainty estimates in LIF measurement

Error source	Uncertainty, %
Shot noise	1.6
Deviation of acetone seeding	2.00
Regulated pressure variance	1.87
Temperature variance	1.02
Total uncertainty	3.3

$$\bar{C}(x,y)=\frac{1}{N}\sum_{i=1}^{N}C_i(x,y);\qquad C_i'(x,y)=C_i(x,y)-\bar{C}(x,y);$$

$$C'_{\mathrm{rms}}(x,y)=\sqrt{\frac{1}{N}\sum_{i=1}^{N}C_i'^2(x,y)};\qquad i=1,\ 2,\ \ldots,\ N;$$

$$r(x,y,\Delta x,\Delta y)=\frac{\frac{1}{N}\sum_{i=1}^{N}[C_i'(x,y)\cdot C_i'(x+\Delta x,y+\Delta y)]}{C'_{\mathrm{rms}}(x,y)\cdot C'_{\mathrm{rms}}(x+\Delta x,y+\Delta y)} \tag{4}$$

Here, point (x, y) is the reference location where the features are correlated, $C_i(x, y)$ is the instantaneous concentration, $C_i'(x, y)$ is its fluctuation, $\bar{C}(x, y)$ is the average concentration, $C'_{\mathrm{rms}}(x, y)$ is the STD of concentration fluctuation, and Δx and Δy are the spatial differences in the x and y directions, respectively. In the present study, the highly significant correlated region (which is the statistically meaningful region) with a sample size N of 500 was where the absolute value of the correlation coefficient $|r| \geq 0.12$, as determined by statistical testing.

D. Resolution of Planar Laser-Induced Fluorescence Images

Since the spatial correlations provide turbulent mixing information on a pixel-sized basis, the spatial resolution of the imaging system and analysis is a key concern in terms of capturing the turbulent behavior. In that sense, we checked the relative resolutions defined by the ratio of the probe dimensions and the mass diffusion scale (Batchelor scale) [8,9], which represents the smallest physical scale at which turbulent mixing is affected by the velocity field. The calculated ratio is about 15, which is the same value as our previous study [1], and it assures that the PLIF data obtained with our imaging system has enough capability of resolving the large-scale flow structures.

E. Estimation of Initial Compressibility Level

Before investigating the convection characteristics of the transverse jets, we estimated the initial compressibility level. In [1], we deduced local convective Mach number distribution for case 1 of the present study from the particle image velocimetry (PIV) data. However, for other cases, we have no velocity data of the flowfields. Therefore, we will estimate a representative value of the convective Mach numbers from the present experimental conditions. Since it is difficult to accurately evaluate the convective Mach numbers representing the compressibility in the flowfield of interest, because of its highly three-dimensional and complex aspects, we therefore follow an idealized model proposed by Gruber et al. [5], which is schematically illustrated in Fig. 1. In this model, they evaluated the convective Mach numbers in zone A, just downstream of the Mach disk of the jet. Thus, the convective Mach numbers obtained here would represent the compressibility effect found in the early stage of mixing. The two streams that form the mixing layer around point A have velocities U_1 (injectant fluid) and U_2 (mainstream fluid). The large-scale eddies in the mixing layer at point A are assumed to be convected with a velocity U_c at an angle parallel to the two constituent streams. To calculate M_c, the Mach number just upstream of the Mach disk (M_1) is necessary. We can determine the pressure downstream of the Mach disk (p_1') using the normal shock and isentropic relations at the Mach disk. Combining these relations with known mainstream conditions (i.e., p_{0m} and M_m) yields an expression for the pressure ratio p_1'/p_m:

$$\frac{p_1'}{p_m}=\left\{\frac{2\gamma_j M_1^2-(\gamma_j-1)}{\gamma_j+1}\right\}\cdot\left\{\frac{[1+1/2\cdot(\gamma_m-1)M_m^2]^{\gamma_m/(\gamma_m-1)}}{[1+1/2\cdot(\gamma_j-1)M_1^2]^{\gamma_j(\gamma_j-1)}}\right\}\cdot\left(\frac{p_{0j}}{p_{0m}}\right) \tag{5}$$

Equation (5) can be used with the prescribed value of p_1'/p_m to derive M_1. Gruber et al. calculated the sensitivity of p_1'/p_m to M_{c1} and concluded that it was not very sensitive. We therefore used the maximum value of M_1, derived by Eq. (5), for the range of p_1'/p_m tested by them and assumed that the velocity U_2 at point A is equal to the velocity component parallel to the one behind the bow-shock wave. The local angle of the bow-shock wave was estimated from the PLIF image of case 1. The convective velocity U_c was calculated from the balance of relative stagnation pressures of the outer and inner flows to the large-scale vortex convected at U_c using the following equation [5]:

$$\left[1+\frac{\gamma_1-1}{2}\left(\frac{U_1-U_c}{a_1}\right)^2\right]^{\gamma_1(\gamma_1-1)}=\left[1+\frac{\gamma_2-1}{2}\left(\frac{U_c-U_2}{a_2}\right)^2\right]^{\gamma_2/(\gamma_2-1)} \tag{6}$$

M_{c1} and M_{c2} at point A are calculated from Eq. (6).

Results obtained by this procedure are presented in Fig. 2 for the cases tabulated in Table 1. Results demonstrated that the air-injection cases had subsonic values (e.g., $M_{c1} = 0.52$ for case 1), while the He-injection cases had supersonic values (e.g., $M_{c1} = 1.71$ for case 5). The local convective Mach number obtained from PIV data for the air-injection case in [1] (the flow condition was the same as case 1) was approximately 0.5 and was very close to the derived convective Mach number of case 1. These comparisons indicate that the convective Mach number estimated with Gruber's model agrees with one obtained from PIV data in the region upstream of the barrel shock. Note that Gruber's model is only reasonable for estimating the initial level of compressibility, because velocity distributions vary locally as the jet flows downstream and are only reasonable for this region.

In general, for $M_{c1} < 0.5$, the turbulent structures are two-dimensional, coherent, and appear as large spanwise rollers. For $M_{c1} > 1.0$, the compressibility effect becomes dominant, and the turbulent structures are smaller in scale, difficult to identify, more three-dimensional, and lack coherence [10,11]. Cases 1 to 4 nearly correspond to the former lower-compressibility condition, and cases 5 to 8 correspond to the latter higher-compressibility condition. Therefore, the experimental conditions in Table 1 are appropriate for

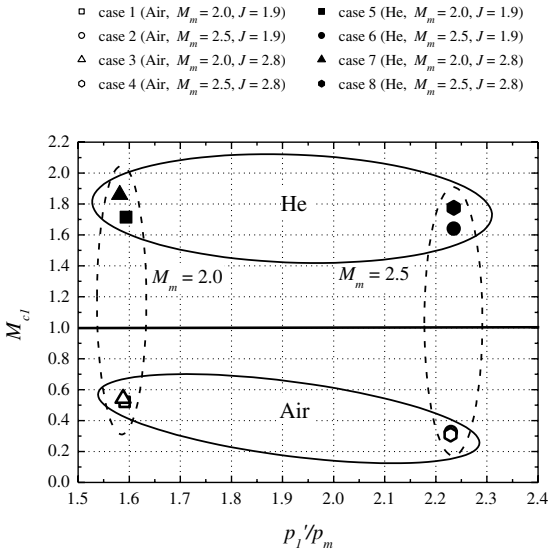

Fig. 2 Results of convective Mach number (M_{c1}) calculations, using a range of pressure ratios in the present experimental conditions.

examining the compressibility effect on the large-scale structure. Note that the velocity difference diminishes as the flow goes downstream, and the local value of the convective Mach number evaluated in [1] may become considerably lower than the convective Mach number estimated above.

III. Results and Discussion

A. Flowfield Visualization and General Features

First, we examine the effects of jet molecular weight on the jet structure at fixed J. Here, we show only one case for each injectant. Figure 3 presents representative instantaneous PLIF images of the side view on the centerplane of the jet in the Mach 2.0 airstream. In the images, the average-concentration tracks at the maximum, 50%, and 10% are plotted with a dotted line, a solid line, and a dashed–dotted line, respectively. Note that the PLIF intensity under this experimental condition is linearly proportional to injectant molar concentration [7]. The roller-type large-scale structure is evident in the air-injection case. On the other hand, it is less evident in the He-injection case. For the reason of this observable difference, some flow instabilities are considered.

Generally, in high-speed flows, the Kelvin–Helmholtz (K–H) instability that is caused from the velocity difference between the jet and the main flow dominates the large-scale turbulent structure, and it results in the formation of the roller-type large eddies. The streamwise velocity distribution in case 1 [1] shows there are velocity differences in the streamwise direction around the 50%-concentration track. Since the roller-type large eddies, evidently seen in the air-injection case, appear around the 50%-concentration track, one of the causes of this structure might be the K–H instability. Another instability caused by density difference between the jet and the main flow, namely, the Rayleigh–Taylor (R–T) instability, might result in the wave interface between the jet and main flow. In general, the R–T instability evolves when lighter fluids contact with heavier fluids under almost constant acceleration normal to the interface, especially from the heavier fluid to the lighter fluid direction. Taking case 1 as an example, because the mean density distribution was provided in [4], the density distribution along the wall-normal direction downstream of $x/D = 3$ indicates the jet fluid is heavier than the main fluid. In addition to this, there is acceleration toward the wall-normal direction, namely, from the jet-to-main flow direction [1], and it continues further downstream. This situation is consistent with the condition where the R–T instability is likely to grow. This consideration in case 1 is roughly applicable to other air-injection cases, because the values of acceleration and density should not be different very much. Although there is no density information other than case 1, the He-injection cases can be expected to have situations opposite to case 1 due to the much lighter molecular weight of helium; the jet fluid is lighter than the main flow fluid. But the transverse velocity distribution of the helium jet may have acceleration in the wall-normal direction from the jet toward the main flow. Therefore, the He-injection cases have the condition where the R–T instability is not likely to grow or, rather, be stabilized. In addition, the helium jet has low density, so that the viscous effect resulting in the penetration and roll up of helium fluids into main flow air fluids did not occur well. These considerations are reasonable to explain why the large-scale structure is likely to occur in the air jet and is not likely to occur in the helium jet.

Next, we examine the effects of the main flow Mach number on the jet structure at fixed J. Figure 4 presents representative instantaneous PLIF images of the side view on the centerplane of the jet in the Mach 2.5 airstream. Comparing cases 1 and 2, the large-scale eddies seem to appear more frequently in case 2 than in case 1. In case 2, because of the faster main flow, the density of the main flow is lower than in case 1; hence, the density difference between the jet and main flow is larger than that of case 1. As a result, the condition of case 2 is more suitable to grow instabilities so that it has large-scale eddies. The opposite trends are seen in cases 5 and 6; namely, the density difference of case 5 is larger than that of case 6. Although these images represent typical instantaneous flow structure of each case, the same trend was commonly observed in the other images. We will quantitatively discuss other turbulent features with the results of statistical analyses later.

Figure 5 presents the distributions of normalized-concentration STD of cases 1 and 5. The STD was normalized by the maximum STD value in the entire region and then normalized again by the absolute maximum-concentration values in each cross section in order to compare the fluctuating level equivalently. The most intensively fluctuating regions appear along the 50%-concentration tracks for both injectant cases. Note that this observation is appropriate for all cases, regardless of the injectant species, M_m, and J. This might prove that the most intensive-concentration fluctuation

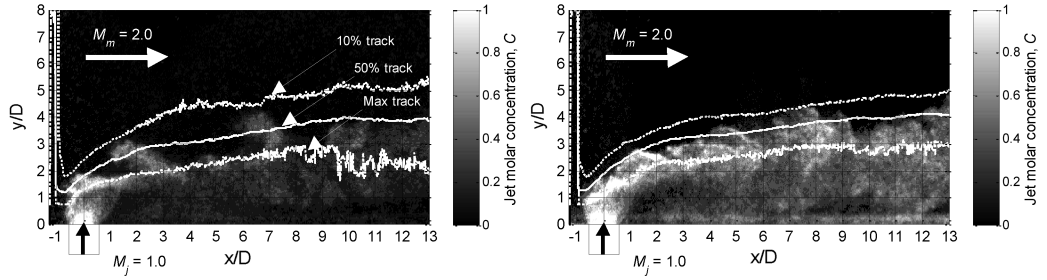

a) Air-injection (case 1) **b) He-injection (case 5)**

Fig. 3 Representative instantaneous PLIF images at centerplane axis of the jet for cases 1 and 5.

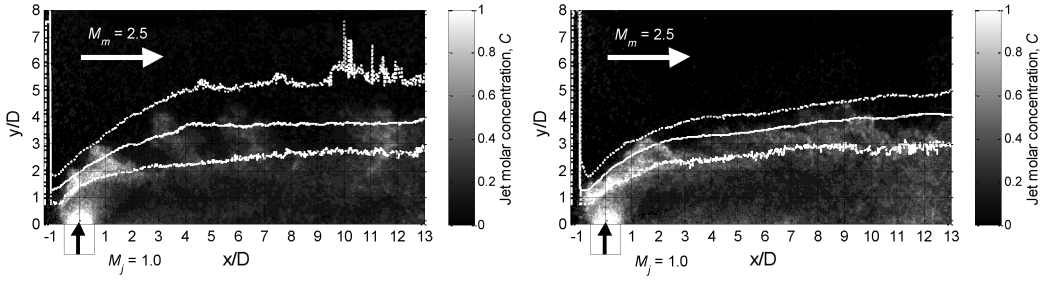

a) Air-injection (case 2) **b) He-injection (case 6)**

Fig. 4 Representative instantaneous PLIF images at centerline axis of the jet for cases 2 and 6.

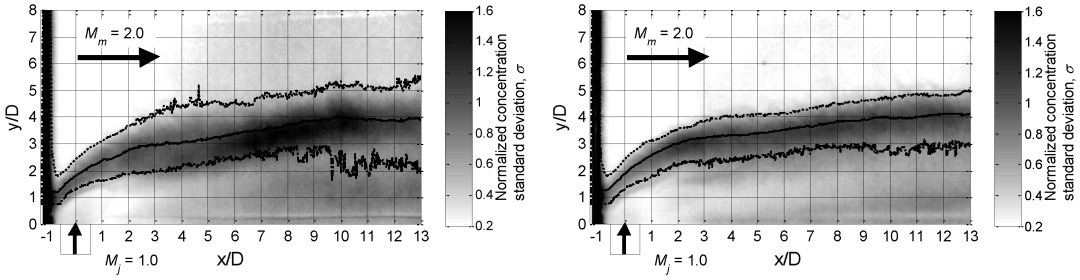

a) Air-injection (case 1) b) He-injection (case 5)

Fig. 5 Normalized STD images of LIF signal for cases 1 and 5.

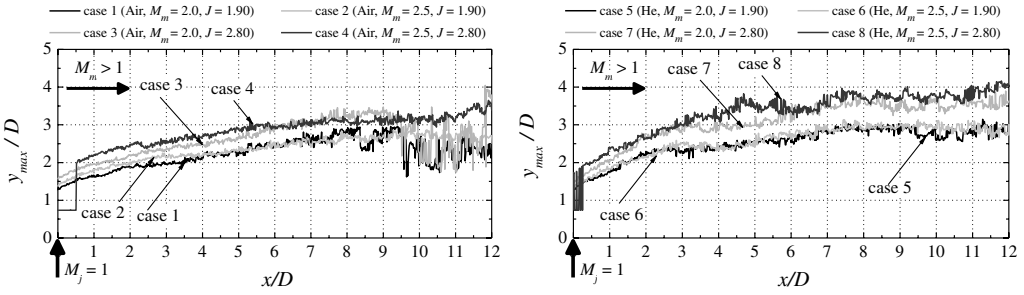

a) Air-injection b) He-injection

Fig. 6 Jet penetration height defined as the maximum-concentration track ($0 \le x/D \le 12$).

mainly resulted from the intermittent motion of the large-scale vortices, since they appeared around the 50%-averaged-concentration track. Taking this fact into account, it is reasonable to investigate the turbulent structure in more detail along the 50% tracks.

Figure 6 depicts the penetration height of the jet into the main flow, defined as the maximum-concentration track. For both injectant cases, the penetration height increases with increasing J. In spite of the same value of J, the He-injection cases penetrate slightly higher than the air-injection cases. Although the Mach disk height may also change between the air- and He-injection cases, due to differences in the specific heat ratio, there is no significant difference in Mach disk height between the air- and He-injection cases shown in Fig. 3. Since the main difference between the air- and He-injection cases is the compressibility and jet velocity resulting from the difference in molecular weight, the jet velocity would cause this difference.

Figure 7 depicts the width of the jet plume between the 10%- and maximum-concentration tracks plotted along the streamwise direction. Lines are smoothed with neighboring points within $0.5D$ for both sides. Generally, the widths increase for $x/D \le 4.5$ and then remain constant for $4.5 \le x/D \le 9$ for both injectants. For $x/D \ge 9$, only the widths of air-injection cases increase again, but those of helium remain constant. These trends differ from the observation in the turbulent mixing layer or the jet injected parallel to the mainstream, where the widths of the mixing layer or jet are increasing in proportion to the downstream distance. Widths of the He-injection cases are generally much narrower than those of the air-injection cases. The widths of the He-injection cases are almost the same, regardless of J or M_m. In contrast, the widths of air-injection cases with higher J and higher M_m are wider than others. In addition, the He-injection cases look smoother than the air-injection cases. The appearance, frequency, and size of the eddies also differ among the different injection cases. Since these observed facts should be related to the turbulent behavior, we will discuss this later with statistical analyses.

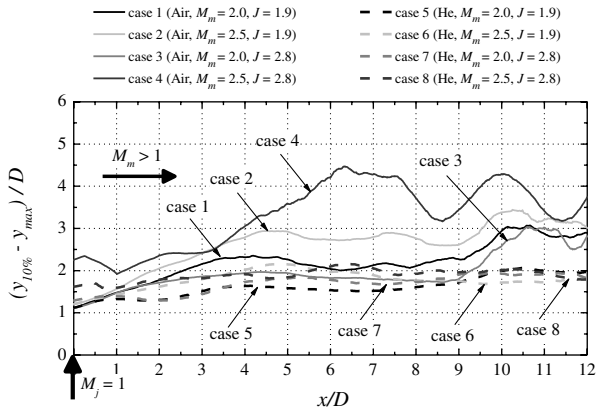

Fig. 7 Width of jet plume between 10%- and maximum-concentration tracks ($0 \le x/D \le 12$).

B. Spatial Correlation

Typical results of computed spatial correlation maps based on the concentration fluctuation for reference points on the 50% tracks are presented in Figs. 8a–8h for cases 1 to 8, respectively. Their reference points were at $x/D = 6$ on the 50% track. In all maps, the main flow direction was from left to right, and the injection point was $x/D = y/D = 0$. Sets of 500 single-shot images were used for computing the correlation. Each correlation map is depicted with the contour levels varying in increments of 0.1 in $0.2 \le |r| \le 1.0$, and the boundary of the highly correlated region ($r = 0.12$) is highlighted with a black solid line.

The large-scale structure was most evidently seen around the 50% track, irrespective of the injection conditions. The air-injection cases in Figs. 8a–8d have tilting elliptic structures against the streamline (considered as the 50%-averaged-concentration track) that appear intermittently, whereas the He-injection cases in Figs. 8e–8h have elliptic structures with the major axes almost parallel to the streamline. According to Kida's stability analysis [12], an elliptic vortex appears in the shear flow, and it rotates, depending on the velocity fields. The stable structure is an ellipse that is parallel to the streamline. In this sense, the He-injection cases generally have stable structures. For every case, the high-correlation regions lie almost between the maximum and 10% tracks. This should result in the formation of the jet boundary width. Since the time-averaged jet

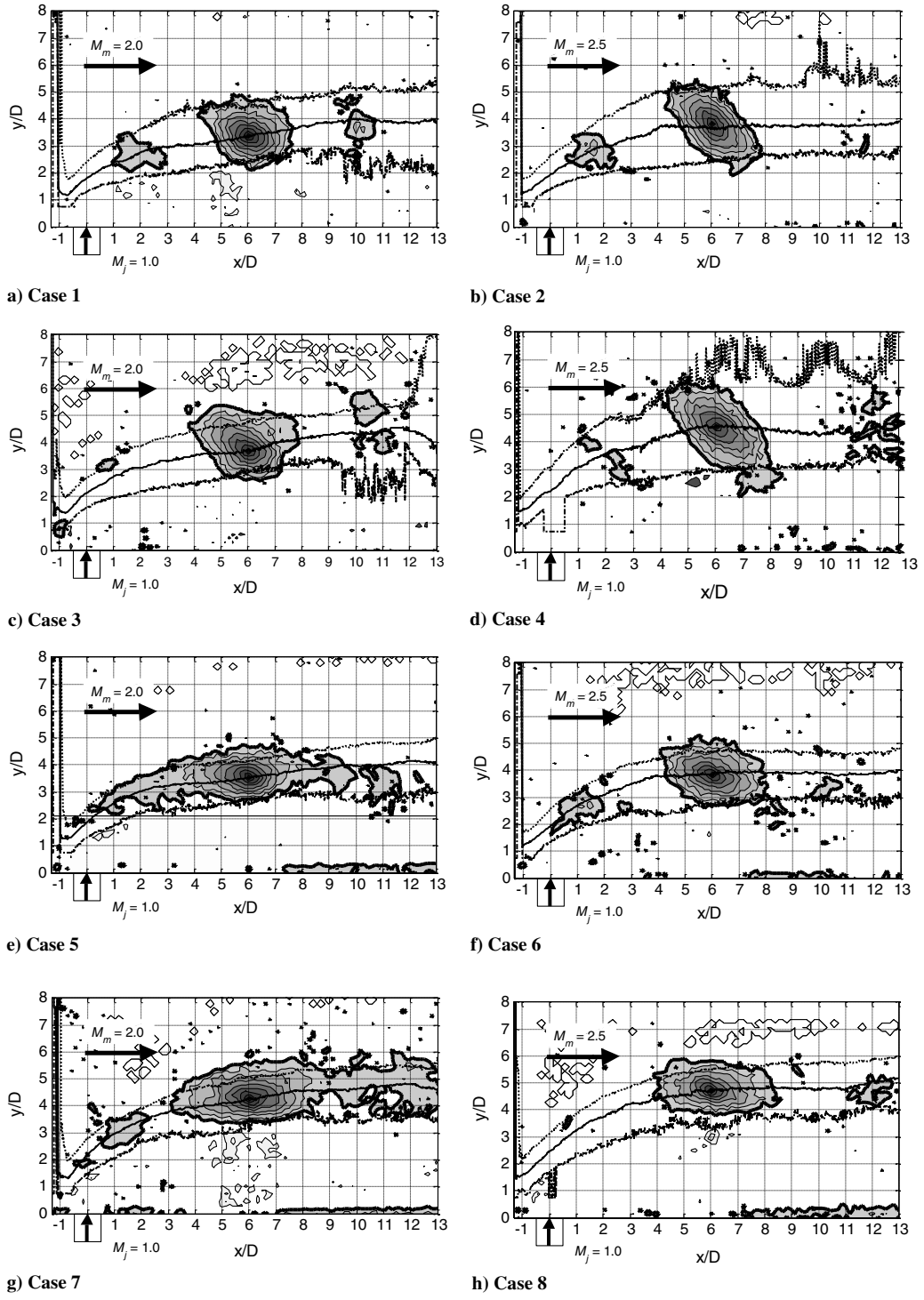

Fig. 8 Spatial correlation maps for air and He injection in the side-view centerplane.

boundary resulted from the shapes and behaviors of instantaneous turbulent structures, the reason why the He-injection cases have narrower widths than the air-injection cases is due to the turbulent structures parallel to the streamline. Therefore, the narrower jet width would represent the more stable flow structures.

Physically, the correlation region for which the contours are concentric circles indicates that the fluctuation at the reference point is isotropic. For cases 1 and 3 at $x/D = 12$ in Fig. 9, the correlation region is almost round, and the maximum trajectory fluctuates significantly. These results indicate the shape changes from a backward-leaning ellipse to a circle because of large-scale flow motions resulting from the change of the velocity field [1].

Qualitatively, the intervals of eddies from the highly significant correlated region can be observed for every case. In case 1, the correlation region appears regularly at intervals of about $4D$. The appearance intervals increased to about $4.5D$ to $5D$ with increasing mainstream velocity (cases 2 and 4). This trend is opposite to one observed in the comparison between Figs. 3a and 4a. The statistical result gives actual features of the turbulent motion found from many realizations, while the instantaneous images provide one particular

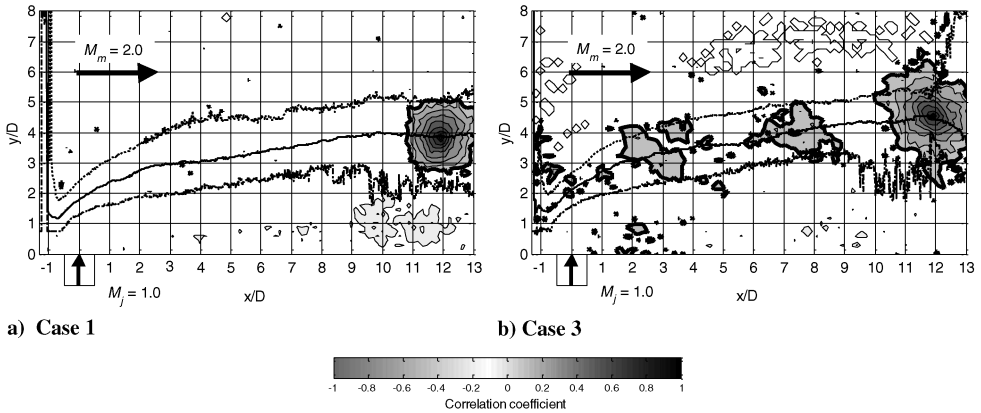

Fig. 9 Spatial correlation maps for air and He injection in the side-view centerplane.

feature of the motion. Therefore, the statistical result is more general and reliable. The intervals with increasing J (case 3) are almost the same as in case 1. In the He-injection cases, the appearance interval ranges are broader than those in the air-injection cases, namely, from $3D$ to $9D$ for cases 6 and 8, and they are not clearly defined for cases 5 and 7 because of elongation of the correlation regions. The cause of the elongated correlation region may be the smaller scale that appears in narrow intervals, or the structure may be inclined in the streamwise direction so that the correlated region appears as an elongated shape. These results may prove that the structure becomes less coherent with increasing compressibility. The appearance interval seems to be dependent on J, because the positions of the highly correlated region in cases 1 and 3 are not very different.

To investigate the geometrical development of the structure quantitatively, a least-squares curve fit [13] was made of each highly correlated region with an ellipse. We discuss the shape, size, and orientation of the ellipse fitted to the correlation regions of $r \geq 0.5$. Figure 10 presents changes in the inclination angles of the major axes plotted along the 50% track for six different cases of each J. For comparison, the subsonic cases that had a main flow Mach number of 0.91 for both injectants are plotted as well.

Obvious axis switching of the fitted ellipse occurred only in case 1 and subsonic cases 9 and 10. In cases of $J = 1.9$, the degree of inclination does not change very much for supersonic cases except case 1. But, the degree is greater in a higher Mach number than in a lower Mach number. In cases of $J = 2.8$, the degree inclination distributes between -15 and -45 deg, and it increases slightly as the structure goes downstream in the air-injection cases. On the other hand, in the He-injection cases, the inclination angle does not change much as $J = 1.9$ but approaches 0 deg for $J = 2.8$. In case 7, although a slight axis switching is seen at around $x/D = 5$, it approaches to zero. In case of $J = 2.8$, the main flow Mach number seems not to have significant influence on the inclination for both injectants, although higher Mach number cases show slightly greater inclinations. With regard to the axis switching, it occurred around $x/D = 5$ to 6, irrespective of injectant species and J in the subsonic condition. On the other hand, in the supersonic condition, obvious axis switching occurred only in the lower-compressibility case with lower J and slight axis switching occurred in the initial stage in the higher-compressibility case with higher J. This means that the axis switching represents a highly unstable flow state, and the unstable state appears around $x/D = 5$ to 6 downstream of the injector. With regard to the extent of inclination, some previous studies [5,11], including wall-injection and mixing-layer investigations, indicate that the large-scale structure in the shear layer is oriented from 25 to 45 deg to the streamwise direction for a low-convective Mach number, namely, $M_c = 0.66$ for [5] and $M_c = 0.745$ for [11]. Our results show that the inclination angle for air-injection cases or lower-compressibility cases is 15 to 60 deg, and it can reach 75 deg, although they are against the streamline direction. Gruber et al. [5] reported that the higher-compressibility case is more likely to rotate or increase the angle while flowing downstream. However, our result in Fig. 10 indicated the opposite trend; the higher-compressibility cases showed a smaller inclination angle; in other words, the structure hardly rotated. Some reasons that caused this difference can be considered. The possible reasons are difference in the measurement technique and streamwise velocity. Gruber et al.'s investigation was done with Mie scattering. The SiO_2/ice particles were used as tracers, and they were introduced into the main flow. The particles may be heavier than the gaseous injectant; hence, the particles would overestimate the real flow path owing to lack of traceability [7,14], especially where the local velocity variance exists. In contrast, PLIF uses gaseous molecules as a fluid marker so that it is capable of following the real flow and represents the real flow

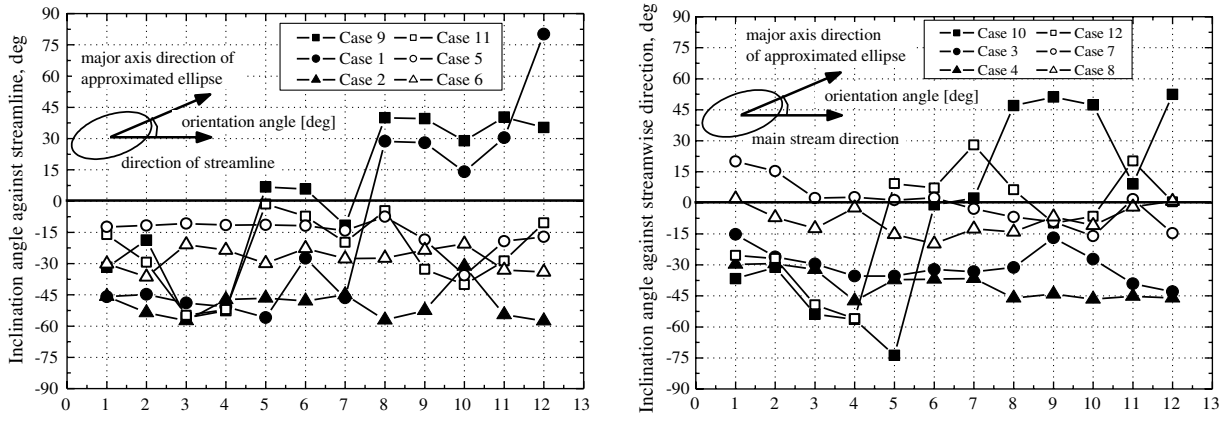

Fig. 10 Change in inclination angle of fitted ellipse along streamwise direction.

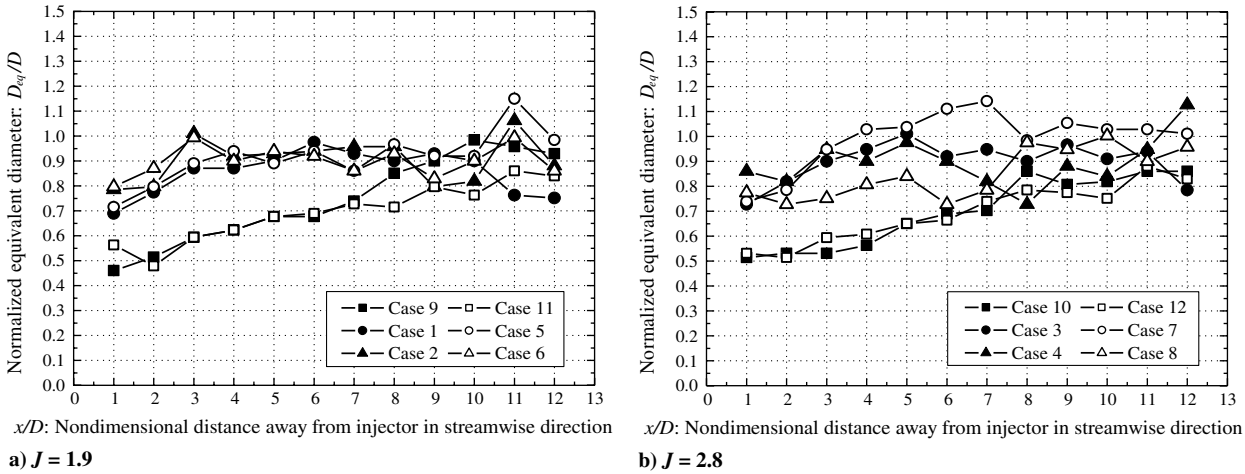

Fig. 11 Equivalent diameter of the area of $r \geq 0.5$.

behavior without any concerns in terms of the traceability. This might cause the disparity by coupling with the other reason. The other possible reason is the difference in streamwise velocity distributions between the present study and Gruber et al.'s investigation [5], since the shape of the correlation region is strongly influenced by the velocity distribution and tends to tilt toward the fast flow direction [15]. The streamwise velocity on the jet-flow side is usually considered to be faster than the main flow side. However, in the present case of transverse injection, the central part of the jet flow passes a Mach disk, and there occurs a large total pressure loss. This pressure loss of the jet-flow results in a wake-type velocity distribution in the air-injection case [6,7]. For the He-injection case, the jet velocity might be faster than the main flow side because of the faster acoustic velocity. Furthermore, the local velocity distribution around the upper jet boundary between our study and Gruber et al.'s [5] in the He-injection case might be different; the streamwise velocity distribution in the jet side in their study might be much faster than the main flow side, whereas the jet and main flow side velocities might be almost the same in our study [1]. Then the elliptic shape of the correlation region for which the reference point was chosen around the 50%-concentration track in their study, results in a highly backward-leaning shape, whereas ours is almost parallel to the streamline. Thus, the disparity in the orientation trend might have happened. Since we did not measure the velocity distribution for the He-injection case, it should be investigated to affirm this explanation.

Figure 11 presents the equivalent diameter distributions obtained from the region of $r \geq 0.5$ ($D_{r\geq 0.5}$) plotted along the streamwise direction for cases 1 to 8. The equivalent diameter was introduced in [1] for the quantitative comparison of the size of the correlation regions. For $J = 1.9$ in the subsonic cases, clearly, the size keeps increasing as it goes downstream; on the other hand, the size reaches a maximum by $x/D = 5$ in the supersonic cases for both injectants. Between air and helium, there is almost no difference until $x/D = 7$, then helium shows a slower increase in the subsonic cases. In the supersonic cases, there is a slight difference, but it is smaller than those of the subsonic cases. The influence of M_m is small in the $J = 1.9$ cases. For $J = 2.8$, the He-injection cases show a larger difference caused from M_m when compared with the air-injection cases for the supersonic cases but, finally, downstream of $x/D = 8$, both air and He are almost the same.

Comparing these results with the results of the PLIF visualizations, increasing the mainstream Mach number increases the appearance interval, the inclination angle, and the size of the large-scale structure, and the structure is likely to be stretched. A linear stability analysis conducted for the mixing layer [16] predicted that the increase of the mainstream Mach number reduces the growth rate and gain along the streamwise coordinate. Our results are consistent with this prediction, although our flowfield was generated by a transverse injection into the supersonic main flow. This result proves the prediction of the linearized theory [16]. To summarize those observations and, taking into account the fact that the higher main flow speed and lighter injectant make a more highly compressible condition, the velocity field made by the main flow velocity field would dominate the convection characteristics of the turbulent structure, especially when the injection momentum is relatively weak. Since we investigated only two conditions in terms of J, the threshold condition of mainstream velocity dominance is not given. Further investigation would be necessary. Moreover, when the jet has higher injection momentum, it more strongly influences the turbulent structure than the main flow does.

IV. Conclusions

We investigated the effects of the jet-to-mainstream momentum flux ratio J, the main flow Mach number M_m, and the injectant species on the development of the large-scale structure. Eight different flow conditions with supersonic main flow and four conditions with subsonic main flow were examined by systematically changing the above-mentioned parameters with the aid of PLIF visualizations and their statistical analyses of the single-time two-point spatial correlations. The following conclusions were drawn.

1) The penetration of the jet is not affected significantly by the main flow Mach number or injectant species. Also, the large-scale structure appears on the 50%-concentration track, irrespective of the main flow Mach number and injectant species.

2) The observable difference in the structure at the jet/air interface between the air-injection and the He-injection cases can be explained by both of the K–H and R–T instabilities.

3) The shape of the large-scale structure identified by the spatial correlation region was a tilting ellipse in the air-injection cases, whereas the shape in the He-injection cases was an ellipse parallel to the streamline. Taking into account the precursor theoretical prediction, the He-injection cases have a stable flow structure. Moreover, the elliptic structure parallel to the streamline results in the narrower averaged jet width.

4) Obvious axis switching was observed in the subsonic and lower mainstream Mach number of the supersonic cases with lower J for air injection. This indicates that the flow condition having lower compressibility and lower J causes axis switching, and it can be translated as the unstable flow condition.

5) The size of the large-scale structure grew until $x/D = 5$, and then it remained constant in the air-injection cases, whereas that of the He-injection cases kept growing slowly throughout the whole observed region. The large-scale structure produced by the He-injection was smaller than that produced by the air injection. The former was likely to be elongated toward the streamline direction.

6) The appearance interval, the inclination angle, and the size of the large-scale structure tended to increase as compressibility decreased. The structure was likely to be stretched toward the averaged-velocity direction as the main flow Mach number

increased. Increasing the velocity difference between the jet and main flows caused the large-scale eddies to appear more frequently.

Acknowledgments

This work was supported by research fellowships of the Japan Society for the Promotion of Science for Young Scientists, through grant 20086092, and by the Grant in Aid for Scientific Research (B) 20360081 of the Ministry of Education, Culture, Sports, Science and Technology.

References

[1] Takahashi, H., Oso, H., Kouchi, T., Masuya, G., and Hirota, M., "Scalar Spatial Correlation in a Supersonic Mixing Flowfield," AIAA Paper 2009-0023, 2009.

[2] VanLerberghe, W. M., Santiago, J. G., Dutton, J. C., and Lucht, R. P., "Mixing of a Sonic Transverse Jet Injected into a Supersonic Flow," *AIAA Journal*, Vol. 38, No. 3, Mar. 2000, pp. 470–479. doi:10.2514/2.984

[3] Billig, F. S., Orth, R. C., and Lasky, M., "A Unified Analysis of Gaseous Jet Penetration," *AIAA Journal*, Vol. 9, No. 6, June 1971, pp. 1048–1057. doi:10.2514/3.49916

[4] Gruber, M. R., Nejad, A. S., Chen, T. H., and Dutton, J. C., "Transverse Injection from Circular and Elliptic Nozzles into a Supersonic Crossflow," *Journal of Propulsion and Power*, Vol. 16, No. 3, May 2000, pp. 449–457. doi:10.2514/2.5609

[5] Gruber, M. R., Nejad, A. S., Chen, T. H., and Dutton, J. C., "Compressibility Effects in Supersonic Transverse Injection Flowfields," *Physics of Fluids*, Vol. 9, No. 5, May 1997, pp. 1448–1461. doi:10.1063/1.869257

[6] Takahashi, H., Ikegami, S., Oso, H., Masuya, G., and Hirota, M., "Quantitative Imaging of Injectant Mole Fraction and Density in Supersonic Mixing," *AIAA Journal*, Vol. 46, No. 11, Nov. 2008, pp. 2935–2943. doi:10.2514/1.37783

[7] Takahashi, H., "Experimental Study of Scalar Structure in a Supersonic Turbulent Mixing Flowfield Using Acetone PLIF," Ph.D. Dissertation, Aerospace Engineering Department, Tohoku Univ., Sendai, Japan, Mar. 2009.

[8] Murugappan, S., Gutmark, E., Carter, C., Donbar, J., Gruber, M., and Hsu, K.-Y., "Transverse Supersonic Controlled Swirling Jet in a Supersonic Cross Stream," *AIAA Journal*, Vol. 44, No. 2, Feb. 2006, pp. 290–300. doi:10.2514/1.13312

[9] Rossmann, T., Mungal, M. G., and Hanson, R. K., "Mixing Efficiency Measurements Using a Modified Cold Chemistry Technique," *Experiments in Fluids*, Vol. 37, No. 4, 2004, pp. 566–576. doi:10.1007/s00348-004-0851-x

[10] Thurow, B., Hileman, J., Lempert, W., and Samimy, M., "A Technique for Real-Time Visualization of Flow Structure in High-Speed Flows," *Physics of Fluids*, Vol. 14, No. 10, Oct. 2002, pp. 3449–3452. doi:10.1063/1.1503802

[11] Mahadevan, R., and Loth, E., "High-Speed Cinematography of Compressible Mixing Layers," *Experiments in Fluids*, Vol. 17, No. 3, 1994, pp. 179–189. doi:10.1007/BF00190915

[12] Kida, S., "Motion of an Elliptic Vortex in a Uniform Shear Layer," *Journal of the Physical Society of Japan*, Vol. 50, No. 10, Oct. 1981, pp. 3517–3520. doi:10.1143/JPSJ.50.3517

[13] Fitzgibbon, A., Pilu, M., and Fisher, R. B., "Direct Least Square Fitting of Ellipses," *IEEE Transactions on Pattern Analysis and Machine Intelligence*, Vol. 21, No. 5, May 1999, pp. 476–480. doi:10.1109/34.765658

[14] Koike, S., Takahashi, H., Tanaka, K., Hirota, M., Takita, K., and Masuya, G., "Correction Method for Particle Velocimetry Data Based on the Stokes Law," *AIAA Journal*, Vol. 45, No. 11, Nov. 2007, pp. 2770–2777. doi:10.2514/1.30962

[15] Ben-Yakar, A., Mungal, M. G., and Hanson, R. K., "Time Evolution and Mixing Characteristics of Hydrogen and Ethylene Transverse Jets in Supersonic Crossflows," *Physics of Fluids*, Vol. 18, 2006, Paper 026101. doi:10.1063/1.2139684

[16] Ragab, S. A., and Wu, J. L., "Linear Instability Waves in Supersonic Turbulent Mixing Layers," *AIAA Journal*, Vol. 27, No. 6, June 1989, pp. 677–686. doi:10.2514/3.10165

R. Lucht
Associate Editor